



HAL
open science

Cenozoic Pb–Zn–Ag mineralization in the Western Alps

maxime bertauts, Adrien Vezinet, Emilie Janots, Magali Rossi, Isabelle
Duhamel-Achin, Philippe Lach, Pierre Lanari

► **To cite this version:**

maxime bertauts, Adrien Vezinet, Emilie Janots, Magali Rossi, Isabelle Duhamel-Achin, et al..
Cenozoic Pb–Zn–Ag mineralization in the Western Alps. *Geology*, 2024, 10.1130/G51818.1 . hal-
04467825

HAL Id: hal-04467825

<https://hal.univ-grenoble-alpes.fr/hal-04467825>

Submitted on 20 Feb 2024

HAL is a multi-disciplinary open access archive for the deposit and dissemination of scientific research documents, whether they are published or not. The documents may come from teaching and research institutions in France or abroad, or from public or private research centers.

L'archive ouverte pluridisciplinaire **HAL**, est destinée au dépôt et à la diffusion de documents scientifiques de niveau recherche, publiés ou non, émanant des établissements d'enseignement et de recherche français ou étrangers, des laboratoires publics ou privés.

1 **Cenozoic Pb–Zn–Ag mineralization in the Western Alps**

2

3 **Maxime Bertauts¹, Adrien Vezinet¹, Emilie Janots¹, Magali Rossi², Isabelle Duhamel-Achin³,**
4 **Philippe Lach⁴ and Pierre Lanari⁵**

5 *¹Univ. Grenoble Alpes, Univ. Savoie Mont Blanc, CNRS, IRD, Univ. Gustave Eiffel, ISTerre,*
6 *38000 Grenoble, France*

7 *²Univ. Grenoble Alpes, Univ. Savoie Mont-Blanc, CNRS, EDYTEM, 73000 Chambéry, France*

8 *³BRGM, F-13276 Marseille, France*

9 *⁴BRGM, F-45060 Orléans, France*

10 *⁵Institut für Geologie, Universität Bern, 3012 Bern, Switzerland*

11

12 **ABSTRACT**

13 Metallogenic models of polyphase mountain belts critically rely on robust geochronology.
14 We combine petrology with Rb–Sr and U–Th–Pb in situ geochronology, paired at thin-section
15 scale, to date mineralization in deformed hydrothermal Pb–Zn–Ag deposits along an east-west
16 transect in the Western Alps, France. The Pb–Zn–Ag veins occur in shear zones with kinematic
17 structures consistent with the mylonitized host rocks. The ore consists mainly of galena in a quartz-
18 phengite gangue. The paragenesis can be related to hydrothermal crystallization during periods of
19 variable strain. Both isotope systems yield only Cenozoic ages (ca. 35 Ma and 15–20 Ma) without
20 any pre-Alpine inheritance, clearly indicating orogenic mineralization. The metallogenic model
21 proposed here includes significant fluid circulation along major tectonic contacts between
22 basement and sedimentary cover during Alpine convergence.

23 INTRODUCTION

24 World-class Pb–Zn–Ag deposits are commonly associated with fluid circulation at
25 basement/cover unconformities in extensive basins (Boiron et al., 2010). However, less-common
26 Pb–Zn–Ag deposits may have an extended evolution influenced by orogenic processes (Williams,
27 1998) that redistributed the ore minerals (Cugerone et al., 2021). Extracting the ages of
28 crystallization and subsequent remobilization of polymetallic ore deposits has proven challenging
29 due to potential reopening of the isotopic systems (Chiaradia, 2023). Dating actinide-rich
30 accessory minerals is the most common and reliable method for obtaining accurate ages because
31 of the possibility to check for concordance using the triple U–Th–Pb decay series (Rasmussen et
32 al., 2006; Li et al., 2019). However, that approach has limitations due to the relative scarcity and
33 small size of accessory minerals suitable for dating (Engi, 2017). The recent development of in
34 situ Rb–Sr dating (Zack and Hogmalm, 2016) on ubiquitous and abundant minerals (e.g., mica,
35 feldspar, apatite) has opened new avenues for constraining the age of deposits as young as $28.1 \pm$
36 2.2 Ma (Şengün et al., 2019). The Rb–Sr method can assess not only the primary age but also
37 subsequent periods of mineralization (Olierook et al., 2020; Tillberg et al., 2021). Proterozoic Rb–
38 Sr ages preserved within Caledonian ore bodies imply inheritance and remobilization during the
39 subsequent orogenic stages (Tillberg et al., 2021).

40 Our study investigates the timing and tempo of Pb–Zn–Ag mineralization along a
41 lithostructural profile in the Western Alps in France, where the tectonic and metamorphic
42 evolution and fluid circulation are well constrained (Handy et al., 2010; Gnos et al., 2021). The
43 abundance of Pb–Zn–Ag mineralization in this area has been attributed to Variscan orogenesis,
44 Mesozoic Tethyan opening, or Alpine remobilization (Nägler et al., 1995). However, recent in situ
45 U–Pb dating by Bertauts et al. (2022) of stratabound Pb–Zn–Ag deposits at Mâcot-la Plagne and

46 Peisey-Nancroix (southeastern France) suggests a new Alpine orogenic period of metallization.
47 To consolidate these results, we used a multi-system approach involving in situ U–Th–Pb and Rb–
48 Sr dating to compare and constrain ages.

49

50 **GEOLOGY AND SAMPLING**

51 Samples were collected along an east-west transect from the Briançonnais domain of the
52 internal Alps to the Belledonne external crystalline massif (Fig. 1). The Briançonnais domain
53 corresponds to the European continental margin and consists of Variscan basement comprising
54 Carboniferous schists and locally some Mesozoic sediments. It was partially subducted under the
55 African tectonic plate before being thrust over the European tectonic plate during the Cenozoic
56 Alpine convergence (Handy et al., 2010). The sedimentary cover is characterized by low-
57 temperature metamorphism (<500 °C) and intense deformation (Strzeczynski et al., 2012). The
58 Belledonne massif is composed of Variscan basement rocks of the European plate, which
59 underwent lower greenschist facies metamorphism and only localized deformation during the
60 Alpine collision (Rossi et al., 2005). The internal metamorphic Alps are separated from the
61 external Alps by the Penninic front, which marks the onset of the European margin collision at ca.
62 35 Ma (Ceriani et al., 2001).

63 We collected 44 samples from mine tailings of seven historic Pb–Zn–Ag deposits. Of these,
64 only four samples from two different lithostructural contexts contain accessory allanite and
65 monazite suitable for U–Th–Pb dating. In the internal Briançonnais domain, one sample from the
66 Peisey-Nancroix deposit is located within the deformed Permian–Triassic cover along the Internal
67 Briançonnais fault (IBF; Fig. 1). In the Belledonne massif, the three samples come from the
68 subsidiary Pb–Zn–Ag mineralization of the Penay and Le Gros Villan deposits, which are located

69 in sub-vertical northeast-southwest dextral shear zones along major faults separating the massif
 70 from the Mesozoic cover (Fig. 1).

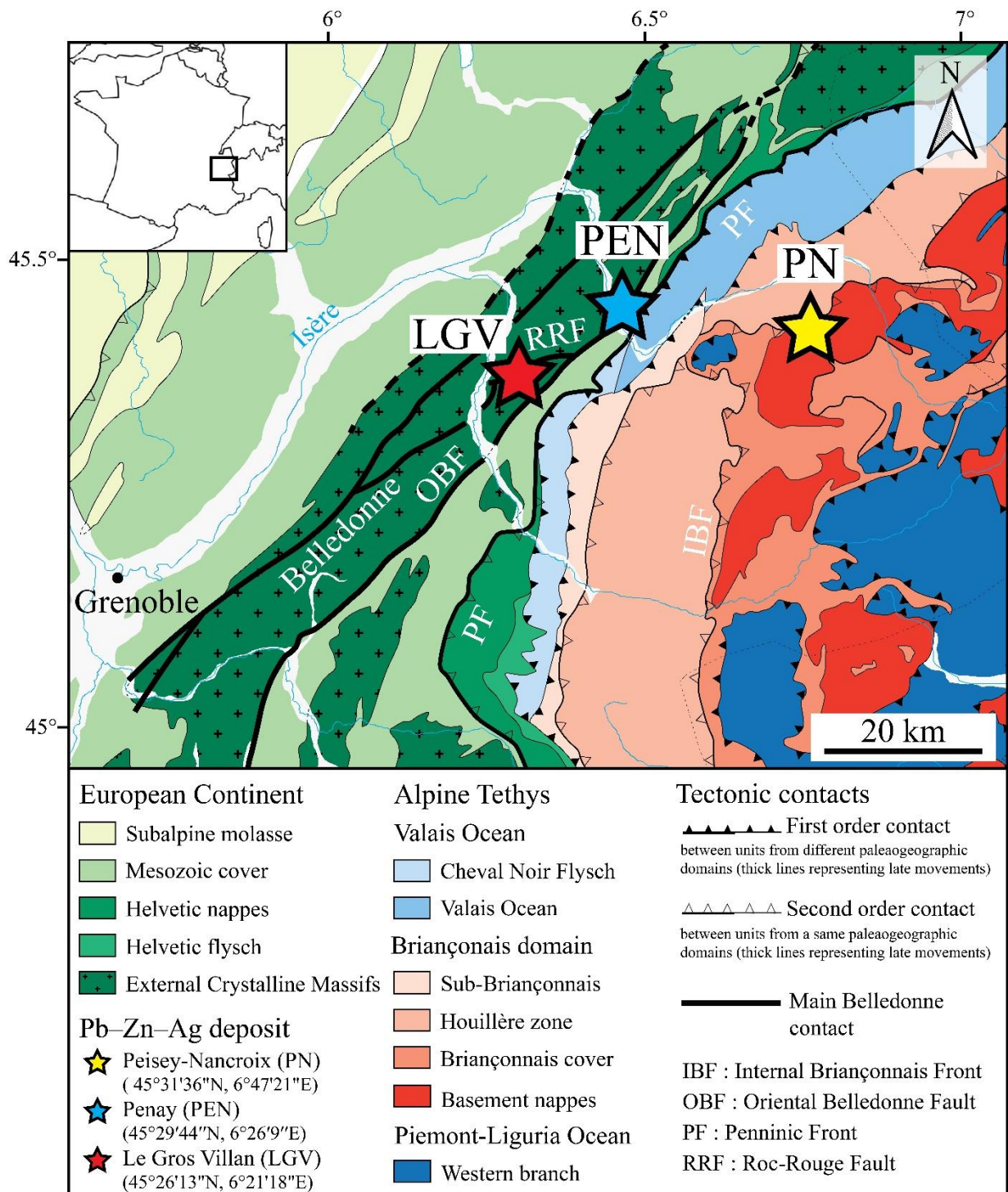


Figure 1. Location of the studied Pb–Zn–Ag mineralizations on the tectonic map of the Western Alps (northern French Alps), modified from Bousquet et al. (2012).

71 **RESULTS**

72 **Mineralogy and Microstructures**

73 The Pb–Zn–Ag mineralization consists mainly of galena with variable amounts of
74 chalcopyrite, sphalerite, tetrahedrite-tennantite, and pyrite. The four samples show evidence of a
75 high-strain regime with clasts hosted in a fine-grained equigranular recrystallized matrix.

76 Based on mineralogy and microstructures (Bertauts et al., 2022), mineralization in the
77 Peisey-Nancroix deposit appears to be synchronous with dynamic quartz recrystallization
78 associated with the precipitation of phengite (Fig. 2A) and monazite (Fig. 2B). The Penay sample
79 shows massive sphalerite in a galena-sphalerite matrix. Clasts of albite, quartz, and foliated
80 phengite aggregates are found within the massive sphalerite and recrystallized matrix (Fig. 2C).
81 Subhedral to anhedral allanite grains are intergrown with sulfides (galena and sphalerite) and
82 phengite contains inclusions of these minerals, indicating a common origin (Fig. 2D). The Le Gros
83 Villan mineralization consists of centimeter-long galena-chalcopyrite-sphalerite-quartz veins
84 hosted in a matrix of recrystallized, partially sericitized quartz and K-feldspar clasts. Phengite that
85 formed at this stage is referred to herein as Ph1. Fractures within the K-feldspar clasts are filled by
86 sulfides (galena and chalcopyrite). Monazite occurs as inclusions within other minerals and forms
87 part of intergrowths with sulfides (Fig. 2F). Hourglass sector zoning within the monazite indicates
88 a single crystallization stage during primary mineralization. The primary mineralization is affected
89 by a second stage of deformation and recrystallization expressed by a foliation made of phengite
90 (Ph2) and secondary fine-grained foliated galena (Gn2) that in places cuts the primary sulfides
91 (Fig. 2E). In these foliated domains, the shape of monazite grains is controlled by foliation
92 deflection of oriented acicular phengite grains.

93

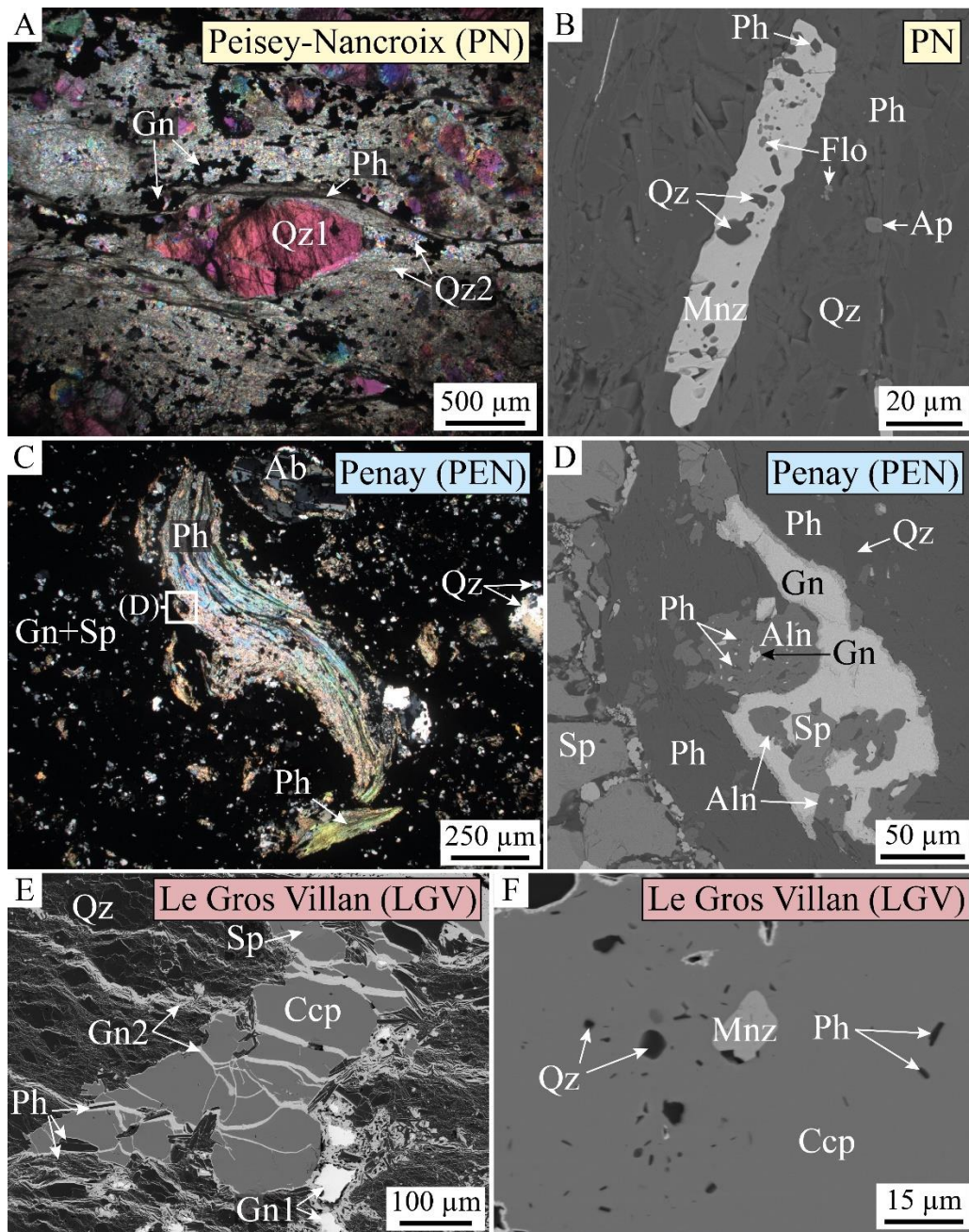


Figure 2. Examples of analyzed phengite (A, C, E) and accessory minerals (B, D, F) used for dating, observed using optical (A, C) and backscattered electron (B, D, E, F) microscopy. The two Peisey-Nancroix samples show: (A) deformed quartz (Qz) Qz1 porphyroclasts shaped by micrometric phengite (Ph) oriented in the foliation, sulfides, and equigranular micrograins of Qz2 (thick section, polarized light) (Gn—galena); and (B) prismatic monazite (Mnz) grain with a poikilitic texture highlighted by quartz, spherical florencite (Flo), and acicular phengite inclusions (Ap—apatite). The massive sulfides from thin sections of Penay show: (C) porphyroclasts of a foliated phengite foliated and folded, albite (Ab), and quartz hosted in a sphalerite-galena matrix (Gn + Sp); and (D) intergrowth texture between galena, sphalerite, and anhedral allanite (Aln) grains within the foliated phengite clast. The sample from Le Gros Villan shows: (E) chalcopyrite (Ccp) cracks filled by oriented acicular phengite and Gn2 crystallization; and (F) subhedral monazite inclusion within chalcopyrite. Abbreviations from Warr (2021).

94 Electron microprobe point analysis and X-ray mapping demonstrated that phengite from
95 the three deposits have homogeneous major and minor element compositions (Table S1 and Figs.
96 S1 and S2 in the Supplemental Material1).

97

98 **In situ LA-ICP-MS Rb–Sr and U–Th–Pb Dating**

99 The U–Pb analyses on 26 monazite grains from the Peisey-Nancroix deposit (Fig. 3A;
100 Table S5) define an isochron in the Tera-Wasserburg diagram that intersects the Concordia at 35.1
101 ± 0.6 Ma (Bertauts et al., 2022). This age is similar to that obtained on 52 in situ Rb–Sr isotopic
102 analyses on five phengite crystal aggregates (Table S8) showing $^{87}\text{Rb}/^{86}\text{Sr}$ values ranging from
103 350 to 800, aligned along an array with a slope corresponding to an age of 34.6 ± 4.7 Ma with an
104 initial $^{87}\text{Sr}/^{86}\text{Sr}$ value of 0.771 ± 0.034 . Two spots have higher Sr contents and Rb/Sr values <70 ,
105 which could correspond to phengite with higher Sr contents or inclusions of Sr-rich minerals such
106 as apatite. When these two spots are added, the resulting isochron gives an older age of 40.1 ± 3.2
107 Ma with an initial Sr isotope ratio of 0.724 ± 0.014 (Fig. 3B).

108 The Th–Pb analyses of allanite from the Penay deposit (Table S7) are plotted in an isochron
109 diagram $^{208}\text{Pb}/^{206}\text{Pbc}$ (c—common) versus $^{232}\text{Th}/^{206}\text{Pbc}$ ($n = 10$, Fig. 3C). The regression
110 yields a Th/Pb age for allanite of 14.9 ± 7.6 Ma. In situ Rb–Sr isotope analyses of three Penay
111 phengite aggregates located within massive sphalerite or fine-grained galena-sphalerite matrix
112 (Table S8) define an isochron age of 18.4 ± 7.2 Ma ($n = 35$) with an initial $^{87}\text{Sr}/^{86}\text{Sr}$ value of
113 0.7214 ± 0.0065 consistent with the Th–Pb age. Six analyses of co-genetic albite grains yield a
114 scattered Sr-isotope weighted mean of 0.7213 ± 0.0030 . When included in the regression, the age
115 remains the same, but the uncertainty of the isochron regression decreases to 3.6 Ma (Fig. 3D).

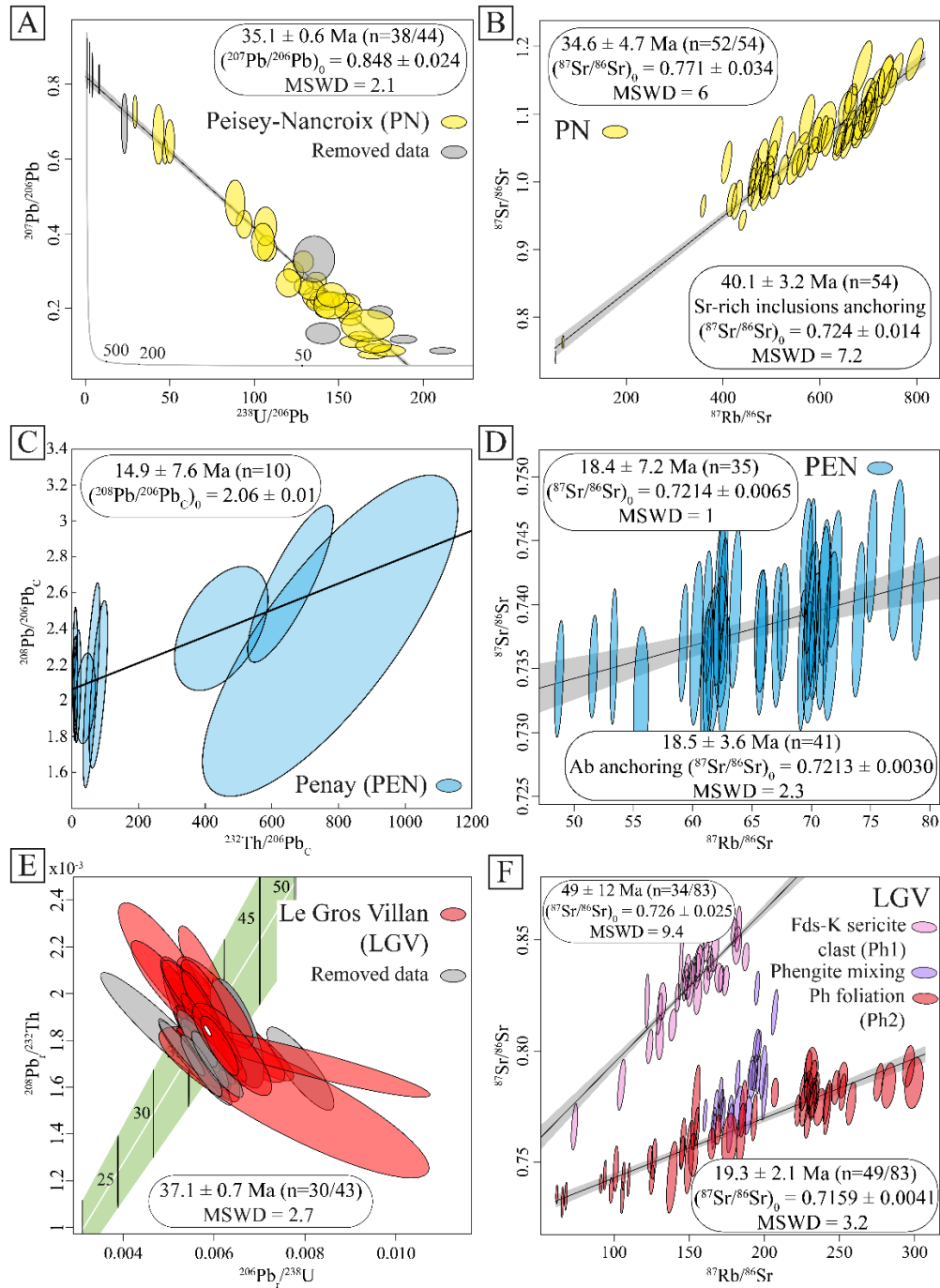


Figure 3. U–Pb (A, C, E) and Rb–Sr (B, D, F) laser ablation–inductively coupled plasma–mass spectrometry analyses on rare earth element–rich phases and phengite (Ph), respectively, for the Peisey-Nancroix (PN) (A, B), Penay (PEN) (C, D) and Le Gros Villan (LGV) (E, F) mineralizations. (A) Tera-Wasserburg diagram of PN monazite without any correction from Bertauts et al. (2022). (C) $^{206}\text{Pb}_c$ normalized Th–Pb isochron of PEN allanite. (E) U–Th–Pb data from LGV monazite are plotted on a $^{208}\text{Pb}_r/^{232}\text{Th}$ versus $^{206}\text{Pb}_r/^{238}\text{U}$ Concordia diagram using the total Pb/U–Th algorithm of Vermeesch (2020). Rb–Sr isochrons and calculated ages for (B) PN sample; (D) PEN sample (Ab—albite); and (F) LGV sample. Fds-K—K-feldspar. Data ellipses represent 2σ errors. MSWD—mean square of weighted deviates.

116 The U–Th–Pb monazite dating from the Le Gros Villan deposit was performed on 22
117 monazite grains obtained from two different thin sections (Table S6). After common Pb correction
118 for the three Pb isotopes (^{206}Pb , ^{207}Pb , and ^{208}Pb), the monazite data yield a Concordia age of
119 37.1 ± 0.7 Ma ($n = 30/43$) on a $^{208}\text{Pb}/^{232}\text{Th}$ (r—radiogenic) versus $^{206}\text{Pb}/^{238}\text{U}$ diagram (Fig.
120 3E). Furthermore, Rb–Sr isotopic analyses were also performed on 10 phengite clusters (Table S8)
121 within sericitized feldspar (Ph1) or secondary foliation (Ph2). All data from the Ph2 foliation align
122 along an isochron that yields an age of 19.3 ± 2.1 Ma. In comparison, the Ph1 results are more
123 complex to interpret, but phengites in one clast plot on a Rb–Sr linear array give an age of 49 ± 12
124 Ma, overlapping the U–Th–Pb age. The other analyses plot between the two isochrons between
125 ca. 49 and 19 Ma (Fig. 3F).

126

127 **DISCUSSION**

128 **Strength of U–Th–Pb and Rb–Sr Geochronology**

129 In fluid-rich environments, the Rb–Sr isochron ages are generally recording the phengite
130 crystallization age (Glodny et al., 2008; Villa, 2016). To prepare the groundwork for in situ dating,
131 careful mineralogical and microstructural relationships were established to determine the
132 crystallization sequences. Homogeneous major and minor elements compositions of phengite are
133 interpreted as one phengite population without recrystallizations (Fig. S1 and Fig. S2). Intergrowth
134 and inclusion relationships (Fig. 2), as well as mineral zoning, indicate that the phengite and REE-
135 minerals are cogenetic. Except Ph2 from the Le Gros-Villan, they coincide with the main stage of
136 sulfide precipitation and thus record the primary age of the Pb–Zn–Ag deposits. Indeed, there is
137 equilibration of the two isotopic systems (Rb–Sr and U–Th–Pb) giving consistent Alpine ages
138 (Fig. 3). Even in the more complex case of the Le Gros Villan deposit, the primary phengite (Ph1)

139 which corresponds to sericitization of K-feldspar, has scattered Rb–Sr isotopic analyses but with
140 a discrete alignment at 49 ± 12 Ma. This older age overlaps with the U–Th–Pb age of the monazite
141 (37.1 ± 0.7 Ma) attributed to the primary mineralization (Fig. 2E, F), with probably some
142 inheritance from K-feldspar. Such results clearly demonstrate the strength of the in situ method
143 used here, because mixing between incompletely reset mica and/or K-feldspar domains has been
144 a recurring problem in solution-based studies (e.g., Müller et al., 1999; Bröcker et al., 2013).

145 The U–Th–Pb dating was complicated by two factors: (i) the scarcity and small size of
146 mineral grains suitable for dating, with only 3 samples out of 44 yielding suitable material, and (2)
147 the possible incorporation of common Pb in this Pb-rich environment, as seen for the Le Gros
148 Villan monazite and, more importantly, for the Penay allanite. In contrast, the ubiquity of mica,
149 the structural control of this mineral, and minimal sample preparation, are advantages of the Rb–
150 Sr system when used for dating of orogenic mineralization. With a wide range of Rb/Sr ratios, in
151 situ dating of white mica can yield a well-resolved Alpine age of $19.3 \text{ Ma} \pm 2.1 \text{ Ma}$ for the Le
152 Gros Villan deposit without isochron anchoring by other phases (10% precision). For samples with
153 lower Rb/Sr spreading (40% precision), isochron anchoring with co-genetic Sr-rich phases
154 improves the precision by about 20%. For samples from the Peisey-Nancroix deposit, isochron
155 anchoring modifies the initial $^{87}\text{Sr}/^{86}\text{Sr}$ value and thus the calculated age, but within the range of
156 uncertainties ($40.1 \text{ Ma} \pm 3.2 \text{ Ma}$ instead of $34.6 \pm 4.7 \text{ Ma}$). The Rb/Sr calibration on the Mica-Mg
157 nano-powder (Tab. S9) may induce a few percent drifted phengite age, but this would represent
158 less than 1 Ma for such young deposit within the uncertainty.

159 Another advantage of cross-comparison of Rb–Sr and U–Th–Pb dating paired in thin
160 section is the ability to distinguish different crystallization stages (Chiaradia, 2023). The primary
161 Eocene mineralization of the Le Gros Villan deposit (37.1 ± 0.7 Ma, monazite) contains secondary

162 phengite (Ph₂) and galena (Gn₂) in post-mineralization microstructures (localized foliation and
163 fractures, Fig. 2E). Thus, Ph₂ in this deposit is thought to record secondary Miocene
164 remobilization at 19.3 ± 2.1 Ma during deformation. In this case, two Rb–Sr ages correspond to
165 two distinct microstructures (Fig. 3).

166

167 **Evidence of Alpine Mineralization and Remobilization**

168 In Peisey-Nancroix, one of the two largest historical Pb–Zn–Ag deposits from the French
169 Alps, the new Rb–Sr dating (Fig. 3B) is consistent with the well-resolved U–Pb syn-orogenic
170 Alpine ages from Bertauts et al. (2022), ruling out a possible sedimentary-diagenetic origin or
171 inheritance for these deposits despite their presence in Triassic quartzite (Rogel, 1961). The
172 deposits formed over a short period of time, which was less than the analytical resolution of in situ
173 U–Pb dating (35.1 ± 0.6 Ma) and Rb–Sr dating (35–40 Ma). The age of ca. 35 Ma is attributed to
174 fluid circulation coeval with the major top-to-west thrusting within the Penninic front (and the
175 Internal Briançonnais front) at the onset of the collision (Strzeczynski et al., 2012).

176 The two deposits in the external crystalline massifs are located in the Variscan basement
177 and show evidence of sulfide recrystallization, suggesting episodic growth and/or remobilization.
178 However, neither in situ U–Th–Pb dating of REE-rich phases nor Rb–Sr dating of white mica
179 indicate a pre-Alpine age. The Miocene ages (15–20 Ma) obtained in these deposits could
180 correspond to the circulation of non-mineralizing fluids (Rolland and Rossi, 2016). The new Late
181 Eocene U–Th–Pb monazite ages in the Le Gros Villan mineralization (Fig. 3E) document early,
182 previously undocumented fluid circulation and are more comparable to those obtained in the
183 internal domains (Gnos et al., 2021). In the external domains, sedimentation had started in a
184 flexural basin, and thrusting in the internal domain along the Penninic front had just begun (Simon-

185 Labric et al., 2009). Thus, early mineralization in the Belledonne massif basement may have been
186 promoted by fluid circulation in Variscan-inherited structures reactivated during burial of the
187 massif (Guillot and Ménot, 2009).

188

189 **CONCLUSIONS**

190 Concordance of the paired in situ Rb–Sr and U–Th–Pb ages in the Western Alps suggests
191 that these isotopic systems reached equilibrium during hydrothermal Pb–Zn–Ag mineralization.
192 The combination of Rb–Sr and U–Th–Pb systems unambiguously indicates Alpine ages for these
193 Pb–Zn–Ag deposits. Two ages, 35–40 Ma and 15–20 Ma, are associated with collision and
194 exhumation of the Belledonne massif. The Rb–Sr geochronological data set obtained on texturally
195 distinctive micas provides evidence for episodic evolution of Alpine Pb–Zn–Ag mineralization.
196 The Pb–Zn–Ag mineralization was produced by fluid circulation along major lithostructural
197 contacts during the Alpine collision.

198

199 **ACKNOWLEDGMENTS**

200 This work was initially supported by the “Référentiel Géologique de la France” RGF-Alps
201 Program of the Bureau de Recherche Géologiques et Minières (BRGM), which financed the Ph.D.
202 grant of M. Bertauts. Additional support was received from the TelluS Program of Centre National
203 de la Recherche Scientifique / Institut national des sciences de l’Univers (CNRS/INSU), the IDEX-
204 Initiative de Recherche à Grenoble Alpes 2021 funding provided by the University Grenoble
205 Alpes, and local BQR funding. The work was mainly carried out at l’Institut des Sciences de la
206 Terre (ISTerre, Université Grenoble Alpes), which is part of the Laboratoires d’excellence
207 (LabEx) OSUG@2020 (ANR10 LABX56). Rb–Sr analyses were conducted in the ISTerre

208 MicroAnalytical Platform (IMAP) at Université Grenoble Alpes, funded by grants from the
209 European Research Council (ERC) under the European Union's Horizon H2020 research and
210 innovation program (Synergy Grant MEET, grant agreement no. 856555); Auvergne-Rhône-Alpes
211 region (2020 AURA P3 – CPER 2015/2020) and CNRS-INSU. We acknowledge the support of
212 the French Agence Nationale de la Recherche (ANR), under grant ANR-23-CE01-0017 (project
213 CMiO). The three anonymous reviewers helped with clarifying several aspects of the paper and
214 are sincerely acknowledged.

215

216 **REFERENCES CITED**

217 Bertauts, M., Janots, E., Rossi, M., Duhamel-Achin, I., Boiron, M.-C., Airaghi, L., Lanari, P.,
218 Lach, P., Peiffert, C., and Magnin, V., 2022, A New Alpine Metallogenic Model for the
219 Pb-Ag Orogenic Deposits of Macôt-la Plagne and Peisey-Nancroix (Western Alps,
220 France): *Geosciences*, v. 12, p. 331, <https://doi.org/10.3390/geosciences12090331>.

221 Boiron, M.-C., Cathelineau, M., and Richard, A., 2010, Fluid flows and metal deposition near
222 basement /cover unconformity: lessons and analogies from Pb-Zn-F-Ba systems for the
223 understanding of Proterozoic U deposits: *Geofluids*, v. 10, p. 270–292,
224 <https://doi.org/10.1111/j.1468-8123.2010.00289.x>.

225 Bousquet, R., Schmid, S.M., Zeilinger, G., Oberhänsli, R., Rosenberg, C., Molli, G., Robert, C.,
226 Wiederkehr, M., and Rossi, P., 2012, Tectonic framework of the Alps: Commission for the
227 geological map of the world (www.geodynamalps.org).

228 Bröcker, M., Baldwin, S., and Arkudas, R., 2013, The geological significance of $^{40}\text{Ar}/^{39}\text{Ar}$ and
229 Rb-Sr white mica ages from Syros and Sifnos, Greece: a record of continuous
230 (re)crystallization during exhumation? *Journal of Metamorphic Geology*, v. 31, p. 629–
231 646, <https://doi.org/10.1111/jmg.12037>.

232 Ceriani, S., Fügenschuh, B., and Schmid, S.M., 2001, Multi-stage thrusting at the “Penninic Front”
233 in the Western Alps between Mont Blanc and Pelvoux massifs: *International Journal of*
234 *Earth Sciences*, v. 90, p. 685–702, <https://doi.org/10.1007/s005310000188>.

235 Chiaradia, M., 2023, Radiometric Dating Applied to Ore Deposits: Theory and Methods, *in*
236 *Huston, D. and Gutzmer, J. eds., Isotopes in Economic Geology, Metallogensis and*
237 *Exploration*, Cham, Springer International Publishing, Mineral Resource Reviews, p. 15–
238 35, https://doi.org/10.1007/978-3-031-27897-6_2.

239 Cugerone, A., Cenki-Tok, B., Muñoz, M., Kouzmanov, K., Olliot, E., Motto-Ros, V., and Le Goff,
240 E., 2021, Behavior of critical metals in metamorphosed Pb-Zn ore deposits: example from
241 the Pyrenean Axial Zone: *Mineralium Deposita*, v. 56, p. 685–705,
242 <https://doi.org/10.1007/s00126-020-01000-9>.

243 Engi, M., 2017, Petrochronology Based on REE-Minerals: Monazite, Allanite, Xenotime, Apatite:
244 *Reviews in Mineralogy and Geochemistry*, v. 83, p. 365–418,
245 <https://doi.org/10.2138/rmg.2017.83.12>.

246 Glodny, J., Kühn, A., and Austrheim, H., 2008, Diffusion versus recrystallization processes in Rb–
247 Sr geochronology: Isotopic relics in eclogite facies rocks, Western Gneiss Region, Norway:
248 *Geochimica et Cosmochimica Acta*, v. 72, p. 506–525,
249 <https://doi.org/10.1016/j.gca.2007.10.021>.

250 Gnos, E., Mullis, J., Ricchi, E., Bergemann, C.A., Janots, E., and Berger, A., 2021, Episodes of
251 fissure formation in the Alps: connecting quartz fluid inclusion, fissure monazite age, and
252 fissure orientation data: *Swiss Journal of Geosciences*, v. 114, p. 14,
253 <https://doi.org/10.1186/s00015-021-00391-9>.

254 Guillot, S., and Ménot, R.-P., 2009, Paleozoic evolution of the External Crystalline Massifs of the
255 Western Alps: *Comptes Rendus Geoscience*, v. 341, p. 253–265,
256 <https://doi.org/10.1016/j.crte.2008.11.010>.

257 Handy, M.R., M. Schmid, S., Bousquet, R., Kissling, E., and Bernoulli, D., 2010, Reconciling
258 plate-tectonic reconstructions of Alpine Tethys with the geological–geophysical record of

259 spreading and subduction in the Alps: *Earth-Science Reviews*, v. 102, p. 121–158,
260 <https://doi.org/10.1016/j.earscirev.2010.06.002>.

261 Li, L.-X., Zi, J.-W., Li, H.-M., Rasmussen, B., Wilde, S.A., Sheppard, S., Ma, Y.-B., Meng, J.,
262 and Song, Z., 2019, High-Grade Magnetite Mineralization at 1.86 Ga in Neoproterozoic
263 Banded Iron Formations, Gongchangling, China: In Situ U-Pb Geochronology of
264 Metamorphic-Hydrothermal Zircon and Monazite: *Economic Geology*, v. 114, p. 1159–
265 1175, <https://doi.org/10.5382/econgeo.4678>.

266 Müller, W., Dallmeyer, R.D., Neubauer, F., and Thöni, M., 1999, Deformation-induced resetting
267 of Rb/Sr and ⁴⁰Ar/³⁹Ar mineral systems in a low-grade, polymetamorphic terrane (Eastern
268 Alps, Austria): *Journal of the Geological Society*, v. 156, p. 261–278,
269 <https://doi.org/10.1144/gsjgs.156.2.0261>.

270 Nägler, Th.F., Pettke, Th., and Marshall, D., 1995, Initial isotopic heterogeneity and secondary
271 disturbance of the Sm-Nd system in fluorites and fluid inclusions: A study on mesothermal
272 veins from the central and western Swiss Alps: *Chemical Geology*, v. 125, p. 241–248,
273 [https://doi.org/10.1016/0009-2541\(95\)00091-Y](https://doi.org/10.1016/0009-2541(95)00091-Y).

274 Olierook, H.K.H. et al., 2020, Resolving multiple geological events using in situ Rb–Sr
275 geochronology: implications for metallogenesis at Tropicana, Western Australia:
276 *Geochronology*, v. 2, p. 283–303, <https://doi.org/10.5194/gchron-2-283-2020>.

277 Rasmussen, B., Sheppard, S., and Fletcher, I.R., 2006, Testing ore deposit models using in situ U-
278 Pb geochronology of hydrothermal monazite: Paleoproterozoic gold mineralization in
279 northern Australia: *Geology*, v. 34, p. 77, <https://doi.org/10.1130/G22058.1>.

280 Rogel, P., 1961, Le gisement de Plomb de La Plagne (Savoie). Etude géologique et métallogénique
281 [Thèse de 3e cycle]: Faculté des sciences de l'université de Paris, 74 p.

282 Rolland, Y., and Rossi, M., 2016, Two-stage fluid flow and element transfers in shear zones during
283 collision burial-exhumation cycle: Insights from the Mont Blanc Crystalline Massif
284 (Western Alps): *Journal of Geodynamics*, v. 101, p. 88–108,
285 <https://doi.org/10.1016/j.jog.2016.03.016>.

- 286 Rossi, M., Rolland, Y., Vidal, O., and Cox, S.F., 2005, Geochemical variations and element
287 transfer during shear-zone development and related episyenites at middle crust depths:
288 insights from the Mont Blanc granite (French — Italian Alps): Geological Society, London,
289 Special Publications, v. 245, p. 373–396, <https://doi.org/10.1144/GSL.SP.2005.245.01.18>.
- 290 Şengün, F., Erlandsson, V.B., Hogmalm, J., and Zack, T., 2019, In situ Rb-Sr dating of K-bearing
291 minerals from the orogenic Akçaabat gold deposit in the Menderes Massif, Western
292 Anatolia, Turkey: Journal of Asian Earth Sciences, v. 185, p. 104048,
293 <https://doi.org/10.1016/j.jseaes.2019.104048>.
- 294 Simon-Labric, T., Rolland, Y., Dumont, T., Heymes, T., Authemayou, C., Corsini, M., and
295 Fornari, M., 2009, $^{40}\text{Ar}/^{39}\text{Ar}$ dating of Penninic Front tectonic displacement (W Alps)
296 during the Lower Oligocene (31–34 Ma): Terra Nova, v. 21, p. 127–136,
297 <https://doi.org/10.1111/j.1365-3121.2009.00865.x>.
- 298 Strzeczynski, P., Guillot, S., Leloup, P.H., Arnaud, N., Vidal, O., Ledru, P., Courrioux, G., and
299 Darmendrail, X., 2012, Tectono-metamorphic evolution of the Briançonnais zone
300 (Modane-Aussois and Southern Vanoise units, Lyon Turin transect, Western Alps): Journal
301 of Geodynamics, v. 56–57, p. 55–75, <https://doi.org/10.1016/j.jog.2011.11.010>.
- 302 Tillberg, M., Drake, H., Zack, T., Hogmalm, J., Kooijman, E., and Åström, M., 2021,
303 Reconstructing craton-scale tectonic events via in situ Rb-Sr geochronology of poly-
304 phased vein mineralization: Terra Nova, v. 33, p. 502–510,
305 <https://doi.org/10.1111/ter.12542>.
- 306 Vermeesch, P., 2020, Unifying the U–Pb and Th–Pb methods: joint isochron regression and
307 common Pb correction: Geochronology, v. 2, p. 119–131, <https://doi.org/10.5194/gchron-2-119-2020>.
- 309 Villa, I.M., 2016, Diffusion in mineral geochronometers: Present and absent: Chemical Geology,
310 v. 420, p. 1–10, <https://doi.org/10.1016/j.chemgeo.2015.11.001>.
- 311 Warr, L.N., 2021, IMA–CNMNC approved mineral symbols: Mineralogical Magazine, v. 85, p.
312 291–320, <https://doi.org/10.1180/mgm.2021.43>.

313 Williams, P.J., 1998, Metalliferous economic geology of the Mt Isa Eastern Succession,
314 Queensland: Australian Journal of Earth Sciences, v. 45, p. 329–341,
315 <https://doi.org/10.1080/08120099808728395>.

316 Zack, T., and Hogmalm, K.J., 2016, Laser ablation Rb/Sr dating by online chemical separation of
317 Rb and Sr in an oxygen-filled reaction cell: Chemical Geology, v. 437, p. 120–133,
318 <https://doi.org/10.1016/j.chemgeo.2016.05.027>.

319

320 ¹Supplemental Material. Analytical methods and monazite U–Th–Pb, allanite Th–Pb, and phengite
321 Rb–Sr data analysis for the Pb–Zn–Ag deposits in the French Northern Alps; chemical map with
322 summary table of the phengite and albite compositions; Tables S1–S8; and Figures S1 and S2.
323 Please visit <https://doi.org/10.1130/GEOL.S.25209137> to access the supplemental material;
324 contact editing@geosociety.org with any questions.